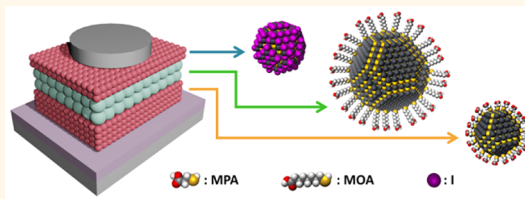# All-Quantum-Dot Infrared Light-Emitting Diodes

Zhenyu Yang,[†] Oleksandr Voznyy,[†] Mengxia Liu,[†] Mingjian Yuan,[†] Alexander H. Ip,[†] Osman S. Ahmed,[†] Larissa Levina,[†] Sachin Kinge,[‡] Sjoerd Hoogland,[†] and Edward H. Sargent*,[†]

[†]The Edward S. Rogers Department of Electrical and Computer Engineering, University of Toronto, 10 King's College Road, Toronto, Ontario M5S 3G4, Canada and [‡]Advanced Technology Materials & Research, Research & Development, Toyota Motor Europe, Hoge Wei 33, Toyota Technical Centre, B-1930 Zaventem, Belgium

ABSTRACT Colloidal quantum dots (CQDs) are promising candidates for infrared electroluminescent devices. To date, CQD-based light-emitting diodes (LEDs) have employed a CQD emission layer sandwiched between carrier transport layers built using organic materials and inorganic oxides. Herein, we report the infrared LEDs that use quantum-tuned materials for each of the hole-transporting, the electron-transporting, and the light-emitting layers. We successfully tailor the

bandgap and band position of each CQD-based component to produce electroluminescent devices that exhibit emission that we tune from 1220 to 1622 nm. Devices emitting at 1350 nm achieve peak external quantum efficiency up to 1.6% with a low turn-on voltage of 1.2 V, surpassing previously reported all-inorganic CQD LEDs.

KEYWORDS: colloidal quantum dots · light-emitting diodes · infrared light emission · carrier transport layers

Since early studies of quantum size-effect tuning in colloidal semiconductor nanoparticles,[1,2] investigations of CQD synthesis, physical chemistry, and applications have advanced at an impressive pace. CQDs are strong candidates for light emission in light of their size-tunable luminescence wavelength, pure color emission, and solution processability.[3−10] The extension of electroluminescence (EL) of CQDs from the visible to the near-infrared (NIR) spectrum with comparatively high quantum yield further suggests their potential for integration in infrared light-emitting diodes (LEDs) for communications,[11] *in situ* bioimaging,[12,13] and gesture recognition.[14] Recent progress in further improving the surface coverage of emissive CQDs, and in balancing of charge injection, has resulted in improved brightness and efficiency of CQD-based NIR LEDs.[15−18] External quantum efficiencies (EQEs) as high as 4.3% have been achieved by using CQDs with thin-shell coverage.[16] Engineering of the interparticle spacing has been achieved by controlling the capping ligand chain length, leading to devices with high EQEs and low turn-on voltages.[15]

CQD IR LEDs have, until now, used device architectures and choices of charge transport layers (CTLs) similar to those employed in visible-emitting counterparts.[6,7,15,16,18,19]

The most frequent choices of materials for hole- and electron-transporting layers (HTL and ETL) are conjugated small molecules and polymers. These inject charges of a first type (electrons/holes), and block charges of a second type (holes/electrons), and are compatible with various processing techniques (*e.g.*, spin-casting, dip-coating and thermal evaporation).[4,16,20−23] Inorganic materials such as metal-oxide and nitride thin films can be integrated into CQD LEDs as the CTLs when they provide the needed band alignment and high carrier mobilities.[24−26] Replacing organic CTLs with inorganic materials has the potential to improve device stability and charge injection.[25,27] However, the performance of all-inorganic devices has been seriously degraded thus far by quenching of the active CQD by the metal oxide layer, and by the imbalanced injection of charges from the two types of CTLs. Moreover, fabrication often requires complex infrastructure and high-temperature processing, compromising the manufacturability benefit of CQD processing.[26] A cost-effective, low temperature process for all-inorganic CQD LEDs is therefore of interest.

Recently, small-diameter metal oxide and quantum dot nanoparticles were incorporated into CQD solids and employed as CTL

materials. Their Fermi energies were controlled using impurity doping and surface ligand exchanges.[28] Benefits such as tunability of the CTLs' bandgaps and high charge carrier mobilities were demonstrated by integrating a CQD-based HTL in planar perovskite photovoltaics.[29] Independent energy band modification of the doping type *via* ligand engineering was shown to improve CQD photovoltaic performance by enhancing carrier collection.[30−33] Even with these significant steps forward for all-inorganic CTLs, only CQD HTLs have been shown. CQDs as ETL materials are so far unexplored, principally because the insufficient charge carrier blocking provided by relatively small-bandgap CQDs. Further, previous CQD CTL work has employed a non-CQD active layer: as a result, the CQD: CQD heterojunction has, until now, been unexplored in the CTL context.

Herein, we fabricate the first CQD-active-layer infrared LEDs that employ a distinct CQD solid for each CTL material. The active layer and CTLs are each CQD solids having the same underlying semiconductor composition, with only nanoparticle size and ligand choice varied to produce the heterointerfaces. These all-CQD devices feature emission wavelengths tunable from 1220 to 1622 nm. Metal halide-based surface treatments improve the CQD ETL in particular, and we use this to reduce the device turn-on voltage. We report EQE values that reach 1.6%. This is over seven times higher than previously reported all-inorganic CQD-based LEDs.[26]

RESULTS AND DISCUSSION

We fabricated devices with CQD-based CTL and active layers directly on a prepatterned indium-doped tin oxide (ITO)-coated glass substrate using solution processing and solid-state surface treatment. PbS CQDs of various sizes were synthesized following an established procedure in which lead(II) oleate and bis(trimethylsilyl) sulfide were used as precursors.[34] CdCl$_2$ treatment was selectively applied during post-synthesis of CQDs used for the active layer and HTL, which allowed for better chloride anion passivation on surface sites and increased photoluminescence quantum yield.[35]

The all-inorganic CQD-based LED architecture was inspired by PbS prior reports of size-dependent band-structure[36] and surface-ligand-induced energy level shifts.[28] We took the view that, through exploitation of quantum confinement and ligand-induced band shifting, we could engineer CQD solids as CTLs. Smaller dots, with larger bandgaps, could be used to ensure charges flowed into a middle layer of larger-diameter quantum dots that would act as the radiative recombination centers. To strengthen carrier blocking properties, we further applied ligand exchange to adjust the electron affinities of these small CQDs, creating a p−n junction to localize charge carriers within the active layer where they would recombine, ideally radiatively.

Our representative device energy band diagram is shown in Figure 1b. The IR emissive active layer, assembled from large-diameter PbS CQDs (nanoparticle diameter ∼4.6 nm, emission wavelength, λ_{em} > 1200 nm), was sandwiched between the ETL and HTL built using CQDs with excitonic absorption wavelengths, λ_{abs}, of 775 and 650 nm (*i.e.*, E_b = 1.6 and 1.9 eV, based on nanoparticle diameter of 2.5 and 2.2 nm, respectively). The solid-state ligand exchange was performed on HTL and ETL PbS CQDs using mercaptopropionic acid (MPA) and tetrabutylammonium iodide (TBAI) solutions, respectively.[28] MPA-treated small CQDs (E_g = ∼1.90 eV) used in the HTL have shallower energy band levels,[28] allowing for efficient hole injection and transport between ITO and emissive large dots. On the ETL side, TBAI treatment and a slight reduction in bandgap (E_g = ∼1.60 eV) push the electron affinity deep enough for injection from a silver electrode.[28] The original oleic acid ligands of the emissive large-diameter dots were exchanged in film using long-chain mercaptooctanoic acid (MOA) ligands, which have been reported by Sun *et al.* to yield a high radiative recombination rate within the active layer.[15] The bandgaps of CQDs were confirmed using absorption spectra (Figure 1c). No obvious shift of λ_{abs} was observed after the ligand exchange and purification processes for any of the CQDs. A cross-sectional scanning electron micrograph (Figure 2a) shows the total thickness of the stacked PbS layers is about 200 nm (HTL, ∼100 nm; active layer, ∼50 nm; ETL, ∼50 nm; Ag cathode, 220 nm). The emission peak can be widely tuned from 1220 up to 1622 nm by changing emissive CQD size (Figure 2b). No significant EL wavelength shift of the devices was observed with respect to the CQD PL spectra. We did not observe EL from devices that used smaller-diameter CQDs as emissive materials (*i.e.*, PL maxima below 1100 nm). This is consistent with the view that Auger recombination increases in smaller dots; meanwhile, a sufficient CTL/emissive layer band-dedge offset is required for efficient charge carrier blocking by the CTLs.

The corresponding results of peak EQE *vs* current density are shown in Figure 2c. The record peak EQE performance of this architecture is 1.58%, achieved by the champion device emitting at 1350 nm. This is over 7 times higher than the best previously published all-inorganic CQD based LEDs.[26,27] The peak EQE values are 0.79%, 0.37%, and 0.14% for devices emitting at 1220, 1450, and 1622 nm, respectively. The current density values at which the peak EQE appears are only slightly different (ranging between 10^{-4} and 10^{-3} A/cm^2) because all active layer CQDs were passivated using the same type of ligand. Similar trends of size-dependent EQE and power conversion efficiency (PCE) performance are noticeable in the average peak EQE values (Figure 2d). Similar to the results reported by Sun *et al.*, our LEDs with MOA-treated emissive dots have much
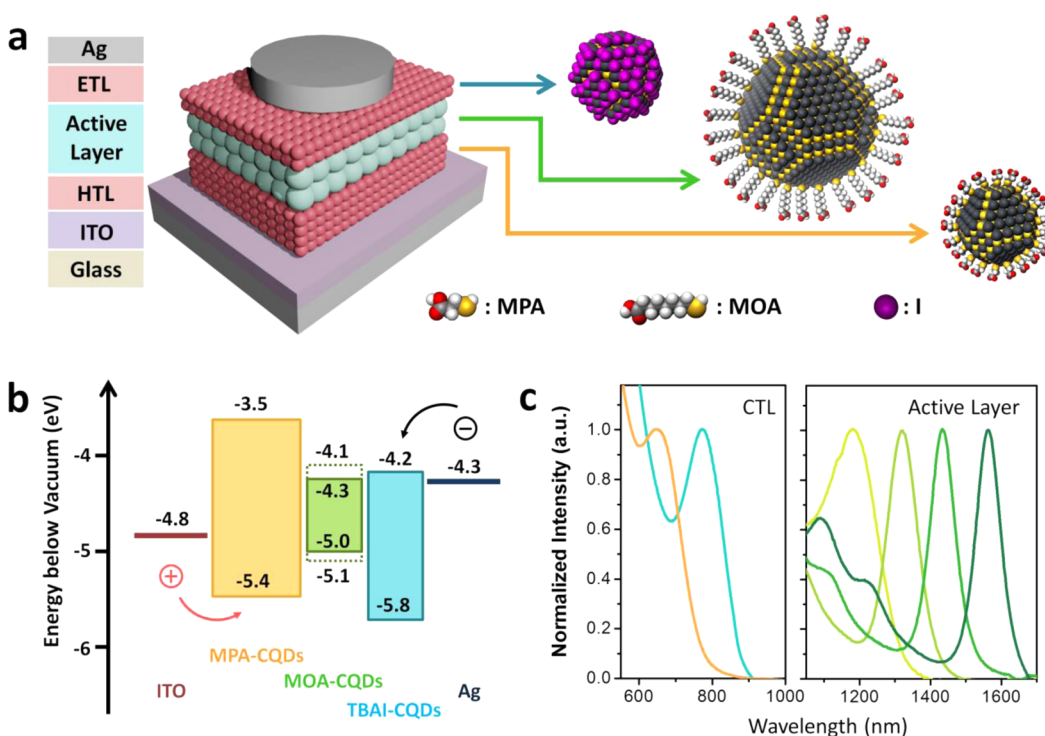
Figure 1. (a) Schematic of the device architecture. Arrows highlight the layers composed of CQDs with different sizes and ligand passivation. (b) Proposed energy level diagram of the CQD infrared LEDs. The energy levels for active layer (MOA-CQDs) correspond to CQDs emitting at 1622 nm (solid line) and 1220 nm (broken line). (c) Absorption spectra of CQDs used for CTLs (λ_{abs} = 650 and 775 nm) and active layer (λ_{abs} = 1178, 1320, 1427, and 1572 nm).
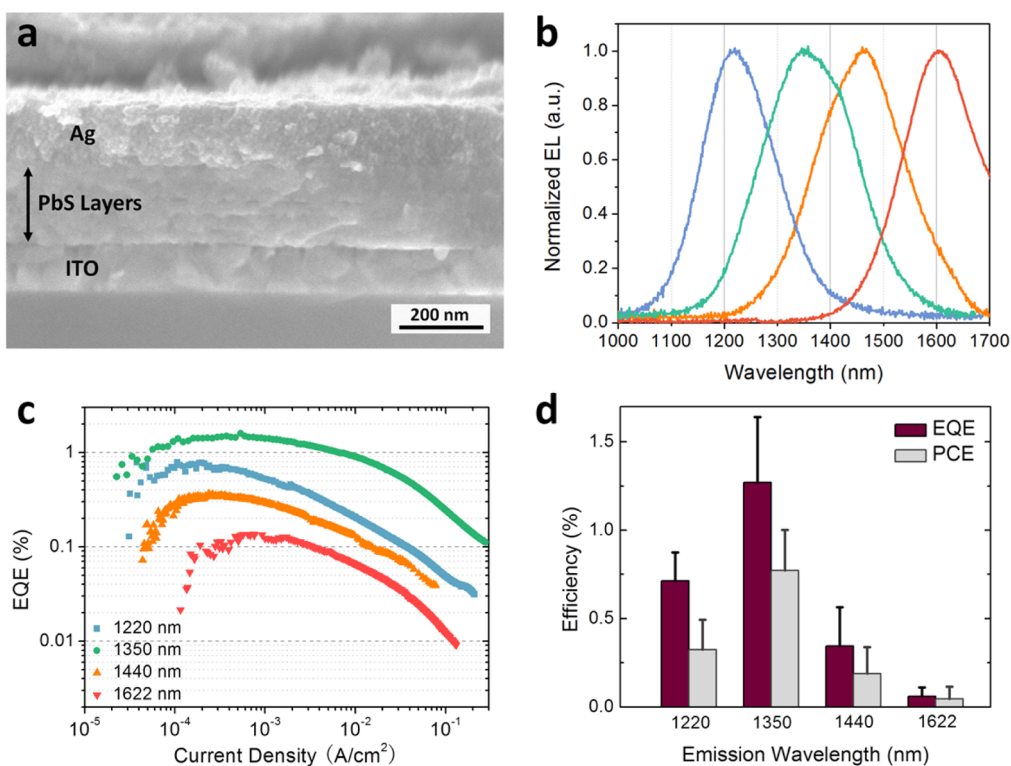

Figure 2. (a) Cross-sectional SEM image of the device with a PbS layer of about 200 nm. (b) Normalized EL spectra of LEDs. (c) EQE-current density performance of champion devices emitting at various wavelengths. (d) Emission wavelength dependent average EQE and PCE values.

higher peak EQE than devices using CQDs treated with shorter MPA ligands in the same architecture (higher peak EQE values by factors of ∼20 to ∼60, depending on the sizes of emissive CQDs), indicating the
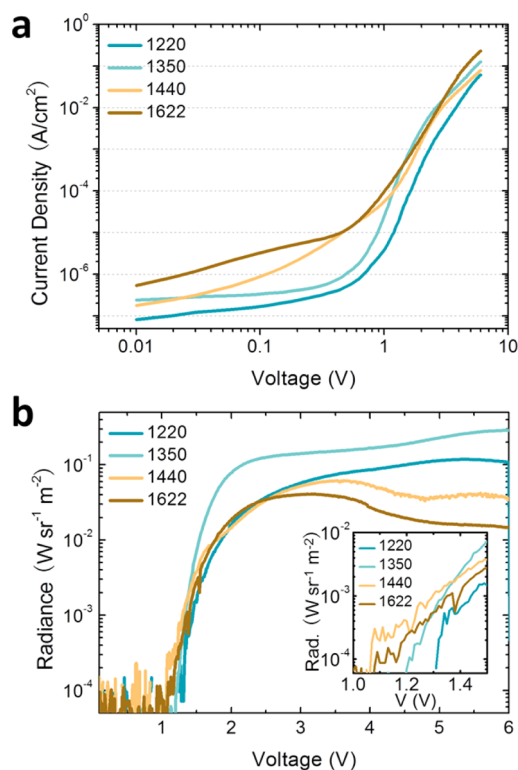
Figure 3. (a) Current density−voltage curves and (b) radiance−voltage characteristics of LEDs emitting in various wavelengths. Inset: zoom-in region of radiance-voltage plots (1.0−1.5 V) showing device turn-on voltages.

TABLE 1. Summary of the electrical Properties of LEDs with Different CQDs as CTLs (Devices Emit at 1350 nm)

E_g of HTL CQDs (eV)	E_g of ETL CQDs (eV)	max EQE (%)	turn-on voltage (V)[a]
1.90 (CdCl$_2$ treated)	1.90	1.12	1.32
1.90 (CdCl$_2$ treated)	1.90 (CdCl$_2$ treated)	0.85	1.26
1.90 (CdCl$_2$ treated)	1.60	1.58	1.20
1.90 (CdCl$_2$ treated)	1.60 (CdCl$_2$ treated)	1.20	1.17
1.60 (CdCl$_2$ treated)	1.60	1.08	1.11
1.60 (CdCl$_2$ treated)	1.60 (CdCl$_2$ treated)	0.71	1.08

[a]:Turn-on voltage is the applied voltage when the EL is detected by the infrared photodetector.

For all particle sizes, the HTL CQDs (*i.e.*, MPA-treated CQDs) were treated using CdCl$_2$ in a postsynthesis step to improve surface passivation and stability against oxidation during low-temperature annealing in air (see Experimental section). We noticed that devices that use larger-diameter CQD-based HTLs had smaller turn-on voltages but lower peak EQEs. This is consistent with the inferior electron-blocking properties provided by larger CQDs due to their smaller bandgap. For ETL preparation, both CQD size and surface passivation were investigated. Devices using ETLs with TBAI-only ligand treatment (*i.e.*, without the addition of CdCl$_2$ during postsynthesis) have higher peak EQE values compared with their counterparts treated using both TBAI and CdCl$_2$. This may be due to the surfaces of CQDs without CdCl$_2$ pretreatment, which have more sites available for iodine incorporation, providing stronger band edge downshifting, and are more beneficial to electron injection and hole blocking. When the ETL is treated using TBAI only, the conduction band offset between the ETL and active layer is smaller; a slightly higher turn-on voltage is consequently observed from such devices. ETLs constructed using slightly larger CQDs have higher EQE values, opposite to what is observed in the HTL study. This may again result from better alignment between the valence bands of the ETL and active layer, which is consistent with the considerably lower turn-on voltages observed in the corresponding devices. To verify the details of recombination modes within these all-inorganic CQD devices, we performed optoelectronic modeling. The simulations (using the SCAPS software suite[38]) are presented in Figure 4 and use material parameters, *e.g.*, trap densities and mobilities, explored previously for CQD photovoltaic devices (see Table S1 for more details).[39] Auger and radiative recombination are included *via* their respective coefficients coupled to quadratic and linear carrier concentrations. Figure 4a shows the band diagram of the device emitting at 1350 nm, above the turn-on voltage, reaching a flat-band condition for efficient carrier injection. The corresponding carrier concentrations are shown in Figure 4b. Some asymmetry in carrier concentration is observed owning to the choice of the electrode
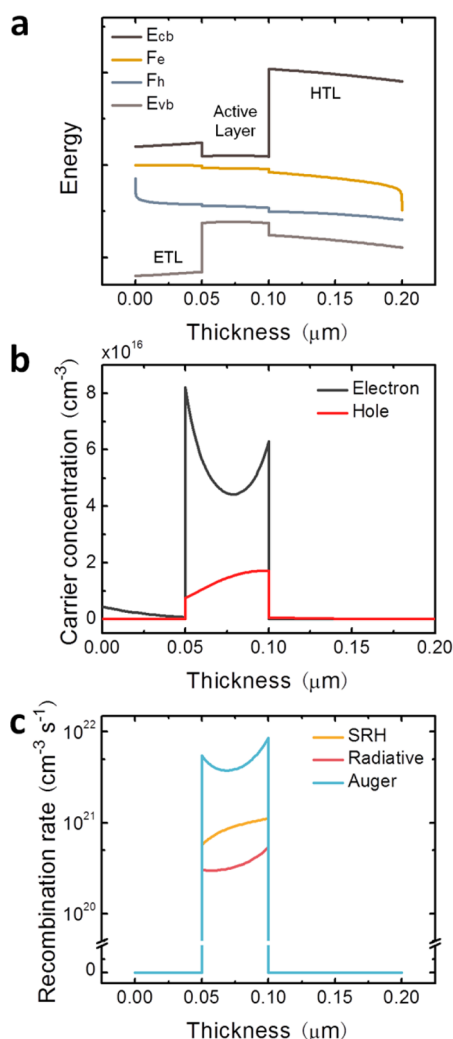
importance of the interdot distance control. The *J*−*V* characteristics of LEDs emitting at various wavelengths are presented in Figure 3a. The devices have ohmic conduction below 0.5−0.7 V depending on the emission wavelength, after which the trap-limited conduction occurs.[37] In the ohmic conduction regime, the current densities of LEDs emitting at 1220 and 1350 nm are strikingly lower, suggesting that current leakage is more effectively prevented using wider-bandgap CQDs. The corresponding radiance *vs* voltage results are shown in Figure 3b. All devices turned on at a voltage between ∼1.05 and 1.32 V (inset figure) with relatively low current density (∼10^{-4} A/cm^2), suggesting these CQD CTLs can effectively inject carriers while providing sufficient blocking. The range of peak radiance of all devices is between 10^{-2} and 10^{-1} W sr^{-1} m^{-2}, and the highest radiance of 0.29 W sr^{-1} m^{-2} was obtained from the device emitting at 1350 nm.

In light of the potential influence of particle size and surface ligand on the performance of small CQD based CTLs, we further conducted a systematic study using our best emissive layer (*i.e.*, CQDs emitting at 1350 nm with MOA passivation) to optimize the ETL and HTL materials. Two sizes of small CQDs (E_g = 1.90 and 1.60 eV) with various surface post-treatments were employed as ETL and/or HTL, and the device peak EQEs as well as turn-on voltages are shown in Table 1.

Figure 4. SCAPS simulation results of (a) band alignment of carrier transport layers and active layers, (b) carrier concentration of electron and hole, and (c) rates of three different types of carrier recombination.

materials and their band alignment relative to the CQD injection layers.

The resulting carrier recombination profile along the device length is presented in Figure 4c. In contrast with CQD LEDs employing organic CTL materials,[40−43] we propose that in our devices, recombination is dominated by Auger processes, with Shockley−Read−Hall (SRH) recombination being secondary and radiative recombination consuming only ∼5% of the injected current. This is expected as Auger recombination is fast in CQDs (∼100 ps) under high-injection conditions. We note that LEDs that use core−shell CQDs as the active material provide a means of decreasing the Auger rate.[16,44] Changing the mobility of the active layer to reflect the change of the ligand length affects mostly the SRH recombination, with higher mobilities (∼10^{-2} cm^2/(V s)) favoring SRH over Auger and PL (Figure S1). When mobility is reduced to ∼10^{-5} cm^2/(V s), carrier transport slows, allowing higher carrier accumulation in the active layer, increasing both radiative and Auger recombination, providing more opportunity for carriers to recombine radiatively or *via* Auger, rendering the relative importance of SRH appreciably lower (Figure 4b,c).

CONCLUSIONS

In this study, we report the first CQD-based infrared LEDs to employ CQD solids for each charge-transporting layer as well as in the light-emitting active material. Band engineering *via* joint control of surface ligand passivation and quantum size tuning of the bandgap enables PbS nanoparticles to multiple key roles in a single LED. Device emission peaks are tailored between 1220 and 1622 nm by changing the emissive dot sizes. The best devices used CQDs emitting at 1350 nm and provided peak EQE reaching 1.58%. Despite significant Auger recombination losses in the shell-free PbS CQDs used here, EQE values and turn-on voltages comparable to the best reported architectures with core−shell CQDs and organic CTLs are achieved. This confirms the best-in-class carrier-transporting and blocking performance of CQD-based CTLs. The simplified material requirements (*i.e.*, single type of material for different functions) and facile solution-based process offer a promising pathway to prepare low-cost and highly efficient CQD-based LEDs.

METHODS

Materials. All chemicals used are commercially available from Sigma-Aldrich (or otherwise specified) and were used without any additional purification steps: lead(II) oxide (99.99%, from Alfa Aesar), cadmium chloride (99.99%), bis(trimethylsilyl)-sulfide (synthesis grade) oleic acid (OA, tech. 90%), 1-octadecene (ODE, ≥95%), oleylamine (≥98%), tetrabutylammonium iodide (TBAI, ≥98%), 3-mercaptopropionic acid (MPA, ≥99%), 8-mercaptooctanoic acid (MOA, 95%) toluene anhydrous, methanol anhydrous, and acetone, distilled in glass (Caledon).

PbS CQD Synthesis and Cadmium Chloride Treatment. Small-diameter PbS CQDs (absorption maximum <785 nm) were synthesized using a well-established hot injection method with some modifications:[34] 0.45 g of PbO, 1.5 mL of OA, 18 mL of ODE, and 0.5 mL of oleylamine were loaded in 250 mL 3-neck round-bottom flask, and then the mixture was pumped at 100 °C for 60 min. After the solution turned optically clear, the temperature was set to the predesigned reaction temperature (60 and 110 °C for dots with absorption peak at 650 and 775 nm, respectively). Then, bis(trimethylsilyl)sulfide ODE solution (0.083 M) was rapidly injected into reaction flask. The heating mantle was turned off (but was not removed) to provide slow cooling. The dots were isolated by addition of 80 mL of acetone and redispersed in anhydrous toluene.

Large PbS dots (absorption maximum >1100 nm) were synthesized according to a recently published method using lead(II) oleate as precursor.[34] Sizes of particles were controlled by the growth time. The solution phase CdCl$_2$ treatment was carried out following a published optimized method.[35] Briefly, 1 mL of CdCl$_2$ (0.06 M) oleylamine solution was injected into the

CQD reaction flask during the slow cooling process. At the temperature below 40 °C, CQDs were precipitated by the addition of ~50 mL of acetone and separated by ultracentrifugation. The supernatant was decanted, and the nanoparticles were redispersed in 2 mL of toluene and transferred into a glovebox. Inside the glovebox, the CQDs were reprecipitated by the addition of an ethanol/methanol mixture (1:1 volume ratio). After the centrifugation, the supernatant was decanted and particles were dried in vacuum for 1 h and then redispersed in octane at a concentration of 50 mg mL^{-1}.

LED Fabrication. The substrate, prepatterned indium tin oxide (ITO)-coated glass, was treated with oxygen plasma for 10 min immediately prior to use. Each functional layer was prepared on the substrate using layer-by-layer spin-coating deposition of CQD:octane solutions with different sizes under air atmosphere at 2500 rpm to obtain each layer of ~30 nm thickness. The HTL consists of four layers of CdCl$_2$-treated small CQDs (absorption maximum at 650 nm) which was spun on ITO substrate and treated with 1% (v/v) mercaptopropionic acid (MPA):methanol solution. Each layer was rinsed with pure methanol twice. Then, the film was annealed at 50 °C under ambient atmosphere for 2 h. After a cooling step to room temperature, two layers of large CQDs (absorption maximum >1200 nm) were spun on with the ligand exchange treatment using 1% (v/v) mercaptooctanoic acid (MOA):acetonitrile solution and spun after 30 s at 1000 rpm. Three rinses with pure acetonitrile were applied for each layer. On top of the active layer, two layers of small CQDs (absorption maximum at 785 nm, without CdCl$_2$ treatment) were spun-cast. Each small CQD layer was treated with 5 mg/mL of tetrabutylammonium iodide (TBAI):acetonitrile solution and spun after 10 s at the same speed for 10 s. Four rinses with pure acetonitrile were applied for each layer. For the top electrode, 220 nm of Ag was deposited by thermal evaporation at a pressure of <1 × 10^{-6} Torr. Each ITO substrate was patterned to yield eight devices, each with an area of 4.9 mm^2.

SEM, EL, and XPS Measurement. SEM characterization were obtained on a Hitachi S-5200 scanning electron microscope. The devices were connected with a Keithley 2410 source meter. Under a range of forward bias voltages, the EL spectra were collected through a set of lenses focused on an optical fiber and connected to an NIR spectrophotometer (Ocean Optics, NIR-512). XPS analysis was carried out using Thermo Scientific K-Alpha XPS system with an Ar ion gun.

Device Performance Characterization. The power of EL was measured using a calibrated Ophir PD300-IR germanium photodiode and recorded *in situ* by a computer-controlled Keithley 2400 source meter under nitrogen atmosphere when the current−voltage (*I−V*) characteristics were measured. Lambertian emission was assumed for EQE calculation, and a geometry correction factor was used according to the distance between photodiode and device and the active area of the detector. Peak EQE was calculated as the number of forward-emitted photons to the number of injected electrons.

Conflict of Interest: The authors declare no competing financial interest.

Supporting Information Available: The Supporting Information is available free of charge on the ACS Publications website at DOI: 10.1021/acsnano.5b05617.

SCAPS simulation results of recombination rates at high mobility of the active layer, and a table that shows the details of SCAPS modeling (PDF)

REFERENCES AND NOTES

1. Efros, A. L.; Efros, A. L. Band-to-Band Absorption of the Light in Semiconductor Sphera. *Fizika Tverdogo Tela* **1982**, *16*, 1209–1214.
2. Rossetti, R.; Nakahara, S.; Brus, L. E. Quantum Size Effects in the Redox Potentials, Resonance Raman Spectra, and Electronic Spectra of CdS Crystallites in Aqueous Solution. *J. Chem. Phys.* **1983**, *79*, 1086–1088.
3. Sargent, E. H. Infrared Quantum Dots. *Adv. Mater.* **2005**, *17*, 515–522.
4. Colvin, V. L.; Schlamp, M. C.; Alivisatos, A. P. Light-Emitting Diodes Made from Cadmium Selenide Nanocrystals and a Semiconducting Polymer. *Nature* **1994**, *370*, 354–357.
5. Coe, S.; Woo, W.-K.; Bawendi, M.; Bulovic, V. Electroluminescence from Single Monolayers of Nanocrystals in Molecular Organic Devices. *Nature* **2002**, *420*, 800–803.
6. Tessler, N.; Medvedev, V.; Kazes, M.; Kan, S.; Banin, U. Efficient Near-Infrared Polymer Nanocrystal Light-Emitting Diodes. *Science* **2002**, *295*, 1506–1508.
7. Steckel, J. S.; Coe-Sullivan, S.; Bulović, V.; Bawendi, M. G. 1.3 to 1.55 μm Tunable Electroluminescence from PbSe Quantum Dots Embedded within an Organic Device. *Adv. Mater.* **2003**, *15*, 1862–1866.
8. Dabbousi, B. O.; Bawendi, M. G.; Onitsuka, O.; Rubner, M. F. Electroluminescence from CdSe Quantum-Dot/Polymer Composites. *Appl. Phys. Lett.* **1995**, *66*, 1316–1318.
9. Mueller, A. H.; Petruska, M. A.; Achermann, M.; Werder, D. J.; Akhadov, E. A.; Koleske, D. D.; Hoffbauer, M. A.; Klimov, V. I. Multicolor Light-Emitting Diodes Based on Semiconductor Nanocrystals Encapsulated in GaN Charge Injection Layers. *Nano Lett.* **2005**, *5*, 1039–1044.
10. Stouwdam, J. W.; Janssen, R. A. J. Red, Green, and Blsue Quantum Dot LEDs with Solution Processable ZnO Nanocrystal Electron Injection Layers. *J. Mater. Chem.* **2008**, *18*, 1889–1894.
11. Klem, E. J. D.; Levina, L.; Sargent, E. H. PbS Quantum Dot Electroabsorption Modulation Across the Extended Communications Band 1200−1700nm. *Appl. Phys. Lett.* **2005**, *87*, 053101.
12. Medintz, I. L.; Uyeda, H. T.; Goldman, E. R.; Mattoussi, H. Quantum Dot Bioconjugates for Imaging, Labelling and Sensing. *Nat. Mater.* **2005**, *4*, 435–446.
13. Lim, Y. T.; Kim, S.; Nakayama, A.; Stott, N. E.; Bawendi, M. G.; Frangioni, J. V. Selection of Quantum Dot Wavelengths for Biomedical Assays and Imaging. *Mol. Imaging* **2003**, *2*, 50–64.
14. Borek, C.; Hanson, K.; Djurovich, P. I.; Thompson, M. E.; Aznavour, K.; Bau, R.; Sun, Y.; Forrest, S. R.; Brooks, J.; Michalski, L.; Brown, J. Highly Efficient, Near-Infrared Electrophosphorescence from a Pt−Metalloporphyrin Complex. *Angew. Chem., Int. Ed.* **2007**, *46*, 1109–1112.
15. Sun, L.; Choi, J. J.; Stachnik, D.; Bartnik, A. C.; Hyun, B.-R.; Malliaras, G. G.; Hanrath, T.; Wise, F. W. Bright Infrared Quantum-Dot Light-Emitting Diodes through Inter-Dot Spacing Control. *Nat. Nanotechnol.* **2012**, *7*, 369–373.
16. Supran, G. J.; Song, K. W.; Hwang, G. W.; Correa, R. E.; Scherer, J.; Dauler, E. A.; Shirasaki, Y.; Bawendi, M. G.; Bulović, V. High-Performance Shortwave-Infrared Light-Emitting Devices Using Core−Shell (PbS−CdS) Colloidal Quantum Dots. *Adv. Mater.* **2015**, *27*, 1437.
17. Choudhury, K. R.; Song, D. W.; So, F. Efficient Solution-Processed Hybrid Polymer−Nanocrystal Near Infrared Light-Emitting Devices. *Org. Electron.* **2010**, *11*, 23–28.
18. Cheng, K.-Y.; Anthony, R.; Kortshagen, U. R.; Holmes, R. J. High-Efficiency Silicon Nanocrystal Light-Emitting Devices. *Nano Lett.* **2011**, *11*, 1952–1956.
19. Bourdakos, K. N.; Dissanayake, D. M. N. M.; Lutz, T.; Silva, S. R. P.; Curry, R. J. Highly Efficient Near-Infrared Hybrid Organic-Inorganic Nanocrystal Electroluminescence Device. *Appl. Phys. Lett.* **2008**, *92*, 153311.
20. Hikmet, R. A. M.; Chin, P. T. K.; Talapin, D. V.; Weller, H. Polarized-Light-Emitting Quantum-Rod Diodes. *Adv. Mater.* **2005**, *17*, 1436–1439.
21. Lee, H.; Kang, C.-M.; Park, M.; Kwak, J.; Lee, C. Improved Efficiency of Inverted Organic Light-Emitting Diodes Using

Tin Dioxide Nanoparticles as an Electron Injection Layer. *ACS Appl. Mater. Interfaces* **2013**, *5*, 1977–1981.

22. Derby, B. Inkjet Printing of Functional and Structural Materials: Fluid Property Requirements, Feature Stability, and Resolution. *Annu. Rev. Mater. Res.* **2010**, *40*, 395–414.

23. Zhao, J.; Bardecker, J. A.; Munro, A. M.; Liu, M. S.; Niu, Y.; Ding, I. K.; Luo, J.; Chen, B.; Jen, A. K. Y.; Ginger, D. S. Efficient CdSe/CdS Quantum Dot Light-Emitting Diodes Using a Thermally Polymerized Hole Transport Layer. *Nano Lett.* **2006**, *6*, 463–467.

24. Caruge, J.-M.; Halpert, J. E.; Bulović, V.; Bawendi, M. G. NiO as an Inorganic Hole-Transporting Layer in Quantum-Dot Light-Emitting Devices. *Nano Lett.* **2006**, *6*, 2991–2994.

25. Caruge, J. M.; Halpert, J. E.; Wood, V.; Bulovic, V.; Bawendi, M. G. Colloidal Quantum-Dot Light-Emitting Diodes with Metal-Oxide Charge Transport Layers. *Nat. Photonics* **2008**, *2*, 247–250.

26. Wood, V.; Panzer, M. J.; Halpert, J. E.; Caruge, J. M.; Bawendi, M. G.; Bulović, V. Selection of Metal Oxide Charge Transport Layers for Colloidal Quantum Dot LEDs. *ACS Nano* **2009**, *3*, 3581–3586.

27. Shirasaki, Y.; Supran, G. J.; Bawendi, M. G.; Bulovic, V. Emergence of Colloidal Quantum-Dot Light-Emitting Technologies. *Nat. Photonics* **2013**, *7*, 13–23.

28. Brown, P. R.; Kim, D.; Lunt, R. R.; Zhao, N.; Bawendi, M. G.; Grossman, J. C.; Bulović, V. Energy Level Modification in Lead Sulfide Quantum Dot Thin Films through Ligand Exchange. *ACS Nano* **2014**, *8*, 5863–5872.

29. Hu, L.; Wang, W.; Liu, H.; Peng, J.; Cao, H.; Shao, G.; Xia, Z.; Ma, W.; Tang, J. PbS Colloidal Quantum Dots as an Effective Hole Transporter for Planar Heterojunction Perovskite Solar Cells. *J. Mater. Chem. A* **2015**, *3*, 515–518.

30. Kramer, I. J.; Sargent, E. H. The Architecture of Colloidal Quantum Dot Solar Cells: Materials to Devices. *Chem. Rev.* **2014**, *114*, 863–882.

31. Ning, Z.; Voznyy, O.; Pan, J.; Hoogland, S.; Adinolfi, V.; Xu, J.; Li, M.; Kirmani, A. R.; Sun, J.-P.; Minor, J.; Kemp, K. W.; Dong, H.; Rollny, L.; Labelle, A.; Carey, G.; Sutherland, B.; Hill, I.; Amassian, A.; Liu, H.; Tang, J.; Bakr, O. M.; Sargent, E. H. Air-Stable N-Type Colloidal Quantum Dot Solids. *Nat. Mater.* **2014**, *13*, 822–828.

32. Yuan, M.; Voznyy, O.; Zhitomirsky, D.; Kanjanaboos, P.; Sargent, E. H. Synergistic Doping of Fullerene Electron Transport Layer and Colloidal Quantum Dot Solids Enhances Solar Cell Performance. *Adv. Mater.* **2015**, *27*, 917–921.

33. Chuang, C.-H. M.; Brown, P. R.; Bulović, V.; Bawendi, M. G. Improved Performance and Stability in Quantum Dot Solar Cells through Band Alignment Engineering. *Nat. Mater.* **2014**, *13*, 796–801.

34. Hines, M. A.; Scholes, G. D. Colloidal PbS Nanocrystals with Size-Tunable Near-Infrared Emission: Observation of Post-Synthesis Self-Narrowing of the Particle Size Distribution. *Adv. Mater.* **2003**, *15*, 1844–1849.

35. Thon, S. M.; Ip, A. H.; Voznyy, O.; Levina, L.; Kemp, K. W.; Carey, G. H.; Masala, S.; Sargent, E. H. Role of Bond Adaptability in the Passivation of Colloidal Quantum Dot Solids. *ACS Nano* **2013**, *7*, 7680–7688.

36. Wise, F. W. Lead Salt Quantum Dots: the Limit of Strong Quantum Confinement. *Acc. Chem. Res.* **2000**, *33*, 773–780.

37. Cho, K.-S.; Lee, E. K.; Joo, W.-J.; Jang, E.; Kim, T.-H.; Lee, S. J.; Kwon, S.-J.; Han, J. Y.; Kim, B.-K.; Choi, B. L.; Kim, J. M. High-Performance Crosslinked Colloidal Quantum-Dot Light-Emitting Diodes. *Nat. Photonics* **2009**, *3*, 341–345.

38. Burgelman, M.; Nollet, P.; Degrave, S. Modelling Polycrystalline Semiconductor Solar Cells. *Thin Solid Films* **2000**, *361−362*, 527–532.

39. Zhitomirsky, D.; Voznyy, O.; Levina, L.; Hoogland, S.; Kemp, K. W.; Ip, A. H.; Thon, S. M.; Sargent, E. H. Engineering Colloidal Quantum Dot Solids within and Beyond the Mobility-Invariant Regime. *Nat. Commun.* **2014**, *5*, 3803.

40. Anikeeva, P. O.; Halpert, J. E.; Bawendi, M. G.; Bulović, V. Quantum Dot Light-Emitting Devices with Electroluminescence Tunable over the Entire Visible Spectrum. *Nano Lett.* **2009**, *9*, 2532–2536.

41. Anikeeva, P. O.; Madigan, C. F.; Halpert, J. E.; Bawendi, M. G.; Bulović, V. Electronic and Excitonic Processes in Light-Emitting Devices based on Organic Materials and Colloidal Quantum Dots. *Phys. Rev. B: Condens. Matter Mater. Phys.* **2008**, *78*, 085434.

42. Anikeeva, P. O.; Halpert, J. E.; Bawendi, M. G.; Bulović, V. Electroluminescence from a Mixed Red−Green−Blue Colloidal Quantum Dot Monolayer. *Nano Lett.* **2007**, *7*, 2196–2200.

43. Bozyigit, D.; Yarema, O.; Wood, V. Origins of Low Quantum Efficiencies in Quantum Dot LEDs. *Adv. Funct. Mater.* **2013**, *23*, 3024–3029.

44. Bae, W. K.; Park, Y.-S.; Lim, J.; Lee, D.; Padilha, L. A.; McDaniel, H.; Robel, I.; Lee, C.; Pietryga, J. M.; Klimov, V. I. Controlling the Influence of Auger Recombination on the Performance of Quantum-Dot Light-Emitting Diodes. *Nat. Commun.* **2013**, *4*, 2661.